Eur. Phys. J. A (2016) **52**: 84
DOI 10.1140/epja/i2016-16084-3

THE EUROPEAN PHYSICAL JOURNAL A

Review

Data analysis for solar neutrinos observed by water Cherenkov detectors*

Yusuke Koshio[a]

Okayama University, 3-1-1 Tsushima-naka, Okayama, Japan

Received: 13 July 2015
Published online: 18 April 2016 –
Communicated by C. Broggini

Abstract. A method of analyzing solar neutrino measurements using water-based Cherenkov detectors is presented. The basic detection principle is that the Cherenkov photons produced by charged particles via neutrino interaction are observed by photomultiplier tubes. A large amount of light or heavy water is used as a medium. The first detector to successfully measure solar neutrinos was Kamiokande in the 1980's. The next-generation detectors, *i.e.*, Super-Kamiokande and the Sudbury Neutrino Observatory (SNO), commenced operation from the mid-1990's. These detectors have been playing the critical role of solving the solar neutrino problem and determining the neutrino oscillation parameters over the last decades. The future prospects of solar neutrino analysis using this technique are also described.

1 Introduction

The ring-imaging water Cherenkov detectors are important for neutrino experiments. The first detector using this technique for solar neutrino detection was Kamiokande (1983–1995) [1]. It confirmed the solar neutrino flux deficit compared to the standard solar model, the so-called the solar neutrino problem. The next-generation detectors were Super-Kamiokande (SK) (1996–) and the Sudbury Neutrino Observatory (SNO) (1999–2006). These detectors played a critical role in solving the solar neutrino problem. The SK experiment is still running, and it measured the first indication of the Earth matter effects by solar neutrino day-night flux asymmetry. The motivations behind future solar neutrino measurement is to investigate the spectrum of up-turn, precise ^{8}B solar neutrino flux, day-night effects, and seasonal variation. One of the proposed experiments is Hyper-Kamiokande, which is a mega-ton-class light water Cherenkov detector.

2 Detection method

The neutrino interactions in the water Cherenkov detectors are as follows:

$$\nu + e^- \to \nu + e^- \qquad (H_2O \text{ and } D_2O), \tag{1}$$

$$\nu_e + d \to p + p + e^- \qquad (D_2O), \tag{2}$$

$$\nu + d \to \nu + p + n \qquad (D_2O). \tag{3}$$

Equation (1) is referred to as neutrino-electron elastic scattering (ES) for both light and heavy water. The charged-current interaction (CC, eq. (2)) and the neutral-current interaction (NC, eq. (3)) occur only for D_2O. The kinetic energy of the charged particles from these interactions can be measured using the detection of photons by photo-multiplier tubes (PMTs). The exact interaction time can also be observed; therefore, several time variation analyses, such as seasonal and day-night difference, are possible.

In the solar neutrino energy region ($\sim$ MeV), the track of the charged particle can be regarded as a point because the track length in water is so small (~ 10 cm) compared to the position resolution of the detector. This point-like position is called a "vertex". The direction of the event is reconstructed from the pattern of the PMTs that observe the photon (hit-PMTs). The angle of the Cherenkov cone in water is 42° for the recoil electron. Though it is not a clear ring image for the solar neutrino event, the distribution of the hit-PMTs has an opening angle that peaks at 42°, and it can be used for direction reconstruction. The number of generated Cherenkov photons is related to the original charged particle energy. For solar neutrino analysis, the number of hit-PMTs is used as a value of the event energy since the number of arrival photons in each PMT is usually one. In the following sections, the detailed analysis methods in SK and SNO are described.

3 Analysis method in Super-Kamiokande

3.1 Brief description of the detector

The SK detector (fig. 1) is a cylindrical tank (39.3 m in diameter and 41.4 m in height) filled with 50 kilotons of

* Contribution to the Topical Issue "Underground nuclear astrophysics and solar neutrinos: Impact on astrophysics, solar and neutrino physic" edited by Gianpaolo Bellini, Carlo Broggini, Alessandra Guglielmetti.

[a] e-mail: koshio@okayama-u.ac.jp

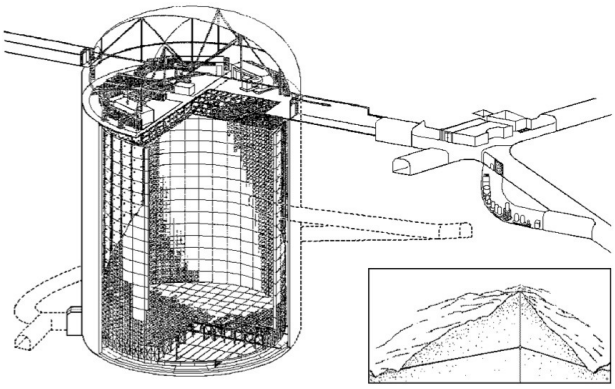

Fig. 1. Super-Kamiokande detector.

pure light water and lined with 11, 129 20 inch PMTs. Due to its large fiducial mass (22.5 kiloton), SK offers the most statistically precise measurement of ^{8}B solar neutrinos. It detects solar neutrinos through the ES interaction; since the electron induced by this reaction preserves the original direction of the neutrino, the solar neutrino signal direction can be clearly seen. The SK detector has been well-calibrated using downward electrons with mono-chromatic energy produced by LINAC calibration [2], $\sim$ 8 MeV gamma-rays produced in DT calibration [3], and $\sim$ 9 MeV multiple gamma-rays produced when a neutron (^{252}Cf source) is captured by nickel (Nickel calibration) [4].

3.2 Vertex reconstruction

Event-position reconstruction is important for separating solar neutrino signals from background events, and its precision affects the fiducial volume determination. To reconstruct the vertex, a maximum likelihood fit to the residual time of the Cherenkov signal as well as the dark noise for each testing vertex is used. The likelihood function is defined as

$$\mathcal{L}(\boldsymbol{x}, t_0) = \sum_{i=1}^{N_{hit}} \log(P(t - t_{tof} - t_0), \qquad (4)$$

where t is the hit time, t_{tof} is the time of flight to the PMT from the vertex, t_0 is the time of the interaction, $\boldsymbol{x}$ is the testing vertex, and P is the probability density function (PDF) obtained from the LINAC calibration data as shown in fig. 2. The position with the largest likelihood is chosen from among the testing vertices as a reconstructed vertex. At first, a trial maximization of likelihood starts from a list of vertex candidates calculated from the PMT hit combinations of four hits each in order to reduce the calculation speed and mis-reconstruction. The four-hit combinations define a unique vertex candidate given their timing constraints. Furthermore, to avoid the local maxima of the likelihood at a position far away from the true vertex, iterations of grid search from 7.8 m to 1 cm around each candidate are performed until they find a position

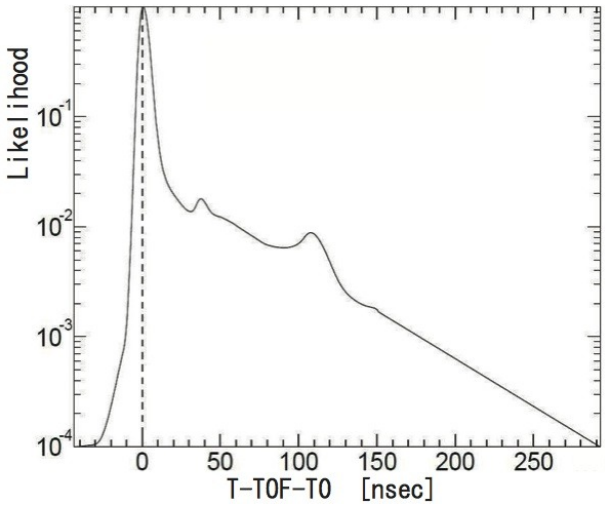

Fig. 2. PDF of residual time for vertex reconstruction. The second and third peaks occur from the after-pulses of the PMTs.

that gives a stable likelihood value. The vertex resolution of this method is $\sim$ 60 cm at 8 MeV.

A bias in the vertex reconstruction between the data and Monte Carlo (MC) simulation, especially a systematic vertex shift, causes systematic uncertainty of the determination of the fiducial volume. By the nickel calibration, the vertex shift was checked at several positions inside the SK tank. It was found to be less than 5 cm at any position.

3.3 Direction reconstruction

Since the pattern of the hit-PMTs has a distinct ring-like angular distribution, the event direction can be reconstructed by scanning all directions and finding that direction which gives the maximum value for the likelihood function. This function is defined as

$$\mathcal{L}(\boldsymbol{d}) = \sum_{i=1}^{N_{20}} \log(f(\cos\theta_{i,E})) \times \frac{\cos\theta_i}{a(\theta_i)}\,, \qquad (5)$$

where N_{20} is the number of hit-PMTs within a 20 ns window around $t - t_{tof} - t_0 = 0$, $f(\cos\theta_{i,E})$ is the expected distribution of opening angles between the direction $\boldsymbol{d}$ and the vector from the reconstructed vertex to the hit-PMT, and $f(\cos\theta_{i,E})$ is obtained from mono-energetic electron MC simulation. Though the likelihood peaks at 42°, the distribution has a wide range expansion. This comes from the electron direction changing due to multiple Coulomb scattering, which depends on the electron energy. The second term in eq. (5) corrects the effect of the photon incident angle to hit-PMT (θ_i) weighted by the PMT acceptance function $a(\theta_i)$. The grid search with sizes from 20° to 1.6° is performed until the likelihood is maximized. The angular resolution is checked by downward electrons produced by LINAC calibration, and it is $\sim$ 25° for 10 MeV electrons.

3.4 Energy reconstruction

It is important to reconstruct the recoil electron energy as precisely as possible since one of the motivations for solar neutrino measurement is to discover the solar neutrino energy spectrum distortion due to neutrino oscillation. The Cherenkov photons emitted by recoil electrons in water will be approximately proportional to the electron energy, and in turn proportional the number of photons observed by the PMT. However, because of the poor charge resolution of the PMTs ($\sim 50\%$) and the fact that only roughly one photon per hit-PMT is detected for electrons below 20 MeV, the energy reconstruction in SK is performed by calculating the number of hit-PMTs with several corrections. The corrected number of hit-PMTs is defined as

$$N_{eff} = \sum_{i=1}^{N_{hit}} \left\{ (X_i + \epsilon_{tail} - \epsilon_{dark}) \times \frac{N_{all}}{N_{alive}} \times \frac{1}{S(\theta_i, \phi_i)} \times \exp\left(\frac{r_i}{\lambda}\right) \times G_i(t) \right\}, \quad (6)$$

where X_i is the correction for the fraction of hit-PMTs that observe multiple photons occurring for events near the wall and at higher energies, and it is determined using Poisson statistics. ϵ_{tail} and ϵ_{dark} are corrections for late hits outside the 50 ns window and dark noise, respectively. The second term shows the bad quality PMT correction. The third term shows the effective photo coverage, which depends on the incident angle toward the surface of the PMT. The fourth and fifth terms show the water transparency and time dependence of the relative PMT gain correction. Since SK is a big detector, water transparency, which is calculated using the amount of observed light from decay electron events produced by stopping muons, is critical for energy reconstruction. Thanks to an improved water purification system, the water transparency is above 120 m in the latest phase. Finally, the total electron energy is calculated as a function of N_{eff} using electron MC simulation as a fourth-degree-polynomial function.

The precision of the energy reconstruction was estimated by comparison between data and MC simulation in LINAC calibration, and the accuracy was better than 0.5%. The energy resolution was estimated by MC simulation and was 14.2% at 10 MeV electron total energy.

3.5 Muon track reconstruction and spallation backgrounds

At the depth of Kamioka site, cosmic ray muons reach the SK detector at a rate of 2.2 Hz. The muon track is reconstructed through the following three steps. First, the entering position is found by the first fired PMT, and the exiting position is found from the center of gravity of the saturated PMT's positions. Next, those positions are iterated by the grid search around the results of the previous step as the hit timing distribution becomes the most likely to be a track. Finally, a geometric check is performed, that is how many saturated PMTs around the reconstructed entering and exit positions to avoid the mis-reconstruction due to the multiple muons. The performance of the muon fitter is estimated by MC simulation. The resolutions of the entrance and exit positions are 68 and 40 cm, respectively. The angular resolution is estimated to be 1.6°.

The energetic muons penetrating water in the detector interact with the oxygen nuclei and produce various radioactive isotopes, known as "spallation products". The energy of β and/or γ particles from the radioactive spallation products is similar to that of recoil electrons from solar neutrinos. The spallation events are correlated in time and space with their parent muon and depend on the muon energy. Therefore, to reject these events, the following three variables are used, *i.e.*, the distance and time differences between a spallation candidate event and the track of the muon and the observed charge from the muons. A likelihood function using the above variables is defined and used to determine whether a spallation event occurs or not.

3.6 Data reduction

Several reduction steps designed to remove the background are applied to the obtained data [5–7]. First, clear noise events, *e.g.*, those caused by electronics noise, are removed using the values of vertex and direction reconstruction quality. The events induced by radioactivity from the PMTs or the detector wall structure are removed using a combination of the vertex and direction. The reduction of gamma rays from ^{16}N (6.13 MeV) generated by cosmic ray muon capture by oxygen are applied using the time correlation to the stopping muon. The usual fiducial volume cut is 2 m from the wall, and the volume is 22.5 kton; however, the radioactive background inside the water is not distributed uniformly. Therefore, an asymmetric fiducial volume cut is applied in the less-than 5.5 MeV energy region, and the volume is 13.3 kton.

3.7 Solar neutrino signal extraction

The angles between the reconstructed direction and the solar direction of the passing events are shown in fig. 3. The solar neutrino signal is extracted using this distribution. The PDF of the signal and background shape are calculated using the simulated and real data, respectively. Signal extraction is performed by an extended maximum-likelihood fit defined as

$$\mathcal{L} = e^{-(\sum_i B_i + S)} \prod_{i=1}^{N_{bin}} \prod_{j=1}^{n_i} (B_i \cdot b_{ij} + S \cdot Y_i \cdot s_{ij}), \quad (7)$$

where N_{bin} is the number of energy bins, n_i is the number of observed events in the i-th energy bin, and Y_i is the fraction of the signal expected in the i-th energy bin made by simulation. The parameters b_{ij} and s_{ij} are background and signal weights as functions of the solar direction, respectively. B_i and S are, respectively, the number of background and signal detections that were finally obtained by the maximum-likelihood method [8].

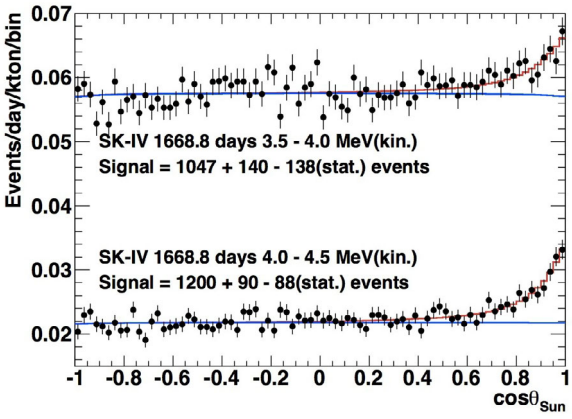

Fig. 3. Solar neutrino signal at the lowest two energy bins in SK-IV. The horizontal axis is the angle between the reconstructed event direction and the vector pointing from the Sun's position to SK when the event happens.

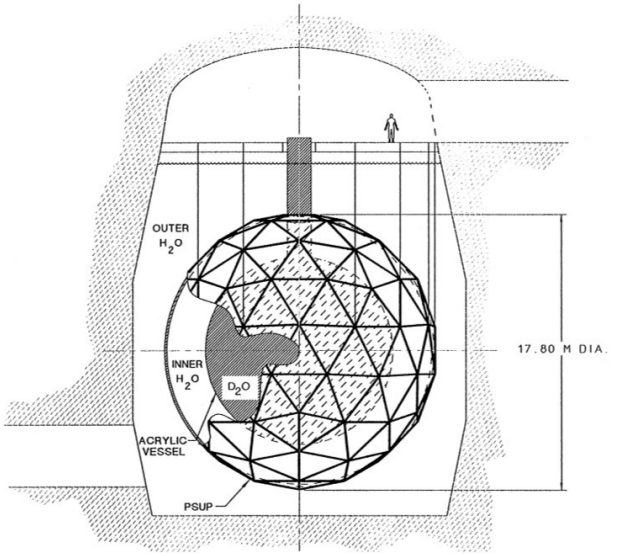

Fig. 4. SNO detector.

3.8 Day-night asymmetry

The day and night solar neutrino flux difference is the cleanest way to see the MSW effect in the Earth. The event rate during the night is expected to be larger since some of the neutrinos produced by $\nu_e \to \nu_x$ oscillations in the Sun will oscillate back into electron neutrinos due to these matter effects. Assuming the current measured neutrino oscillation parameters, this effect is just $\sim 3\%$ in the SK energy region; therefore, huge statistics are needed to see any significant effect. In fact, the solar neutrino flux in night-time is significantly larger than that in day-time at SK. The asymmetry defined as $A_{DN} = (\text{day-night})/\frac{1}{2}(\text{day} + \text{night})$ is $-4.1 \pm 1.2 \pm 0.8\%$. The significance of non-zero day-night asymmetry is $2.8\,\sigma$.

In addition to the straightforward method mentioned above, high accuracy analysis was introduced. The additional scaling factor of the day-night asymmetry expected due to the Earth matter effects was taken into account in the signal extraction likelihood function. The likelihood function in eq. (7) is modified as

$$\mathcal{L} = e^{-(\sum_i B_i + S)} \prod_{i=1}^{N_{bin}} \prod_{j=1}^{n_i} (B_i \cdot b_{ij} + S \cdot Y_i \cdot s_{ij} \cdot z_i(\alpha, t)), \qquad (8)$$

where z_i is the signal time variation factor that depends on the time t and the scaling factor of the day-night asymmetry α. z_i includes the effect of the Earth matter-enhanced neutrino oscillation. After a maximum-likelihood fit to the data is performed and α is obtained, this α factor is finally applied to the expected day-night asymmetry [9]. The observed asymmetry in this method was $-3.3 \pm 1.0 \pm 0.5\%$ (3.0σ) assuming neutrino oscillation parameters by solar neutrino global analysis [10].

4 Analysis method in the SNO

4.1 Brief description of the detector

The SNO was the first and only heavy water (D_2O) Cherenkov detector (fig. 4). The heavy water can measure the solar neutrino signal via all the interactions of eqs. (1) ES, (2) CC and (3) NC, independently. Cherenkov photons from the electrons produced by ES and CC were detected by the PMTs; here, the total number of observed photons was correlated with the incident neutrino energy. For detecting NC events, generated neutron tagging was a key issue. The SNO experiment had three phases which were distinguished by how neutrons from NC interactions were detected. In the first phase, a single 6.25 MeV gamma ray generated by neutron capture on deuterons was used. The gamma ray made Cherenkov photons by secondary Compton electrons and/or positrons. In the second phase, 2 kilotons of NaCl were loaded in D_2O. Neutrons were captured on ^{35}Cl nuclei, which had a larger capture cross-section and higher energy release (8.6 MeV) than deuterium. In the third phase, an array of helium-3 proportional counters for direct neutron detection was deployed in D_2O.

The SNO had an improved analysis method year after year, and the combined analysis of all three phases was eventually presented [11–13]. To extract the neutrino signals from the remaining background, the following four variables were used, *i.e.*, the effective electron kinetic energy, the cube of the reconstructed radial position of the event, the reconstructed direction of the event relative to the direction of the Sun, and the isotropy of the detected light. These values were useful for statistically separating the interaction types as follows. The observed kinetic energy came from the specific electron energy produced by solar neutrino interactions via CC and ES. The electron direction was strongly correlated with the incident neutrino direction in ES, while it was anti-correlated with the

incident neutrino direction as $1 - 1/3\cos\theta$ in CC, where θ was the angle between the neutrino and electron directions. Since the neutron capture via NC reaction produced several gamma rays and the CC and ES reactions produced single electrons, the Cherenkov light from neutron captured events was more isotropic than from CC and ES events. In the following sections, the reconstruction method is related to the four abovementioned variables.

4.2 Vertex and direction reconstruction

4.2.1 Reconstruction method

The fiducial volume of the SNO detector is a spherical shape with a radius of 550 cm inside an acrylic vessel. The precision of the vertex reconstruction directly affects the uncertainty of the determination of the fiducial volume. Furthermore, since many types of external background events increase with radius, a good position resolution allows for them to be more efficiently rejected. Finally, an accurate position measurement provides a better separation of the NC reaction from others because the spatial correlation between the prompt positron signal and delayed gamma ray events due to neutron capture is important in identifying the NC reaction.

The direction information can be used for the separation of each reaction in the SNO. The recoil electron direction is strongly correlated with the incident neutrino direction in ES, whereas the electron via CC has a slightly higher probability to be emitted backward, and the event via NC has a flat angular distribution.

The SNO followed several steps for the vertex and direction reconstruction and used different algorithms in the various cases of the detector.

The first stage of the vertex reconstruction used a maximum-likelihood method with the residual time:

$$\mathcal{L} = \prod_{i=1}^{n_{hits}} P_{ver}(t_i^{res}), \tag{9}$$

$$t_i^{res} = t_i^{PMT} - t^{fit} - \frac{|\boldsymbol{x}^{fit} - \boldsymbol{x}_i^{PMT}|}{c_{avg}}, \tag{10}$$

where t_i^{PMT} is the PMT hit time, t^{fit} and $\boldsymbol{x}^{fit}$ are the fitted time and testing position, respectively, $\boldsymbol{x}_i^{PMT}$ is the position of the hit-PMT, and c_{avg} is the average group velocity of light in water. The PDF P_{ver} was generated by MC simulation of low-energy background events in the light-water region.

Once the vertex was determined, the direction was fitted by a maximum-likelihood method. The likelihood function was defined as follows:

$$\mathcal{L} = \prod_{i=1}^{n_{sel.hits}} P_{dir}(\theta_i) \frac{\cos\phi_i(\boldsymbol{x}^{fit})}{(\boldsymbol{x}_i^{PMT} - \boldsymbol{x}^{fit})^2}, \tag{11}$$

where P_{dir} is the PDF of Cherenkov photon generation, which was determined by 5 MeV electron MC simulation. The last term shows the acceptance as a function of the photon incident angle (ϕ) into the i-th hit-PMT.

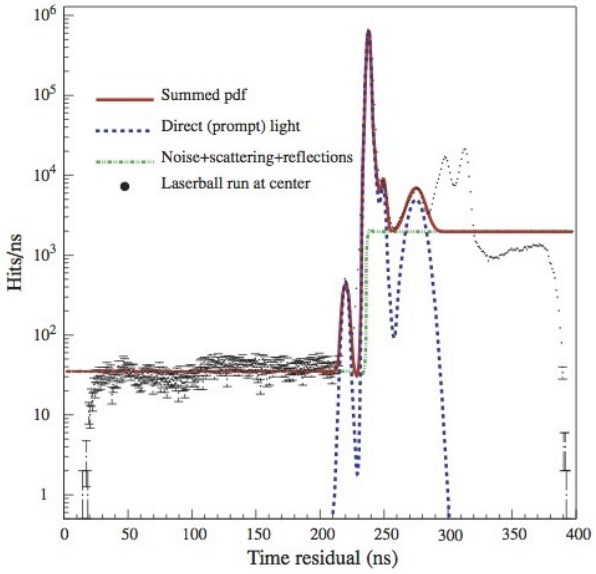

Fig. 5. PMT hit time distribution in the laserball calibration. The dashed and dotted lines show the PDFs of direct and non-direct lights, respectively.

The $n_{sel.hits}$ shows the number of hit-PMTs used for the direction reconstruction, and selected with a time residual window of ± 10 ns to avoid the effect of scattered light in this stage.

The vertex and direction were reconstructed separately; however, this may lead a reconstruction uncertainty due to ignoring angular information while fitting the vertex. In the next step, the likelihood function was modified to simultaneously include both vertex and direction as follows:

$$\mathcal{L} = \prod_{i=1}^{n_{hits}} \mathcal{P}\left(t_i^{res}, \boldsymbol{x}_i^{PMT}; \boldsymbol{x}^{fit}, \boldsymbol{v}^{fit}, t^{fit}\right). \tag{12}$$

The direct light and the other light contributions are separately considered in the probability $\mathcal{P}$. The weights of these two contributions were obtained by the laserball calibration runs, *i.e.*, the direct light was 0.879 and the other light was 0.121. Each probability was divided into time and angle factors. The time factor was also obtained by the laserball calibration data. The direct light time factor included the PMT pre-pulse, signal peak whose width due to the PMT time resolution (~ 1.5 ns), late pulse, and the PMT after pulse. The non-direct light time factor was the step function of flat random PMT noise for $t^{res} < 0$ and random noise in addition to an average contribution from reflected and scattered light for $t^{res} > 0$. Figure 5 shows the residual time distribution from the laserball calibration data overlaid with the probability functions. Since most of the hit-PMTs observed single photons, the Poisson probability was used as the angle factor in $\mathcal{P}$. It consisted of an expected number of photons and the acceptance function in each hit-PMT. The photons that were out of the Cherenkov cone due to scattering tended to reconstruct the event vertex downstream of the true position. To compensate for this systematic shift, the vertex was corrected to move back along the direction.

In the neutron counter phase, the shadowing effect of the counter string was considered in the likelihood function. For this purpose, the PDF of the time residual was separated into two components, *i.e.*, direct and shadowed, depending on the light paths from the event position to the PMT. The PDF was generated by electron MC simulations.

4.2.2 Uncertainties of the reconstruction

The quality of the vertex reconstruction was estimated using ^{16}N calibration data. The average of the reconstructed position relative to the source position was compared to the value from the simulation data. The difference in the position shift between data and MC had a 4 cm spread in the three directions, and the mean shift from data to MC was < 6 cm in z direction, which was equivalent to a $\pm 1\%$ scaling of the reconstructed event radial position. For data analysis, this vertex shift uncertainty was separately estimated in two components: one was the offset, which was independent of the position and estimated by the center position calibration data, the other was the scale, which was position-dependent bias.

The position resolution was also calculated by ^{16}N calibration data and MC and was 15–20 cm at 10 MeV electron in all the axis. The resolution of the calibration data was 1–5 cm broader than the simulation. This effect was applied for signal extraction by smearing the positions of all MC events.

The angular resolution was estimated by MC simulation. It was defined as the angle between the true and reconstructed direction that contained 68% of the angular distribution and $\sim 25^\circ$ for 10 MeV electrons. The uncertainty of the angular resolution was estimated using the Compton-scattered electron from ^{16}N gamma. Since the gamma energy was sufficient compared to the rest mass of the electron, the electron was scattered in the forward direction relative to the incident gamma direction. Therefore, the direction of the scattered electron could be determined by the vector from the source and reconstructed position. The angular distribution of the ^{16}N calibration data was in good agreement with the simulation, and the angular resolution uncertainty was estimated to be 11%.

4.3 Energy reconstruction

The number of hit-PMTs was used to estimate the event energy. In the early stage of the SNO, the number of hits within ± 10 ns of prompt time peak in the PMT residual time distribution, which was the direct photon component and accounted for $\sim 88\%$ of all hits, was used as an initial value N_{win}. The corrections to the noise hits, optical response, hardware status, and time variation of the collection efficiency were applied to N_{win}. The conversion from the corrected N_{win} to the energy was calculated by mono-energetic electron MC simulation. The reconstructed energy distribution of the ^{16}N calibration data was in good agreement with the MC simulation.

For lowering the energy threshold analysis, not only the prompt time peak but also the late hits were used as energy estimators. The event kinetic energy (T) was obtained by the maximum likelihood method. For that purpose, the number of Cherenkov photons (N_γ) was estimated since it was related to the original electron kinetic energy, and an electron with kinetic energy could make an N_γ distribution. Next, the expected number of hits was estimated when the N_γ photons were emitted. This number was separated based on the following five sources: direct photons, Rayleigh-scattered photons in D_2O or H_2O, reflected photons off the surface of the acrylic vessel, reflected photons off the surface of the PMTs or light concentrators, and the PMT noise hits. The probabilities of the each of the above sources except for the PMT noise were computed by MC simulation of photons propagating through the detector. The total expected number of hits (N_{exp}) could be calculated by the product of N_γ and the probabilities corrected for the multi-photon effect of the direct photons and the PMT noise hits. The probability of observing a particular number of hits (N_{hit}) when N_{exp} were expected was given by the Poisson distribution. Finally, the likelihood function was defined by integration over the distribution of N_γ at a given kinetic energy (T):

$$\mathcal{L}(T) = \int \frac{(N_{exp})^{N_{hit}} e^{-N_{exp}}}{N_{hit}!} \times P(N_\gamma|T) \mathrm{d}N_\gamma, \qquad (13)$$

where $P(N_\gamma|T)$ was the probability that the number of emitted Cherenkov photons was N_γ in the case of an event with kinetic energy T. After the above energy reconstruction, several corrections (*e.g.*, the spatial energy scale correction and linearity corrections) were applied, as the ^{16}N energy distribution matched the MC simulation at several source locations. The corrections were evaluated from the data, *e.g.*, the time-variation of the energy response and z-axis dependence of the energy scale.

The uncertainties related to the energy reconstruction were those of energy scale and energy resolution. They were determined by comparing data and MC simulation of ^{16}N calibration. Several sources were studied, and the total systematic uncertainty for the scale was 1.04%. The resolution uncertainty induced by spatial variation was 1.04% and the resolution shift by the temporal stability was 1.19%.

4.4 Event isotropy

The solar neutrino events via CC and ES were single electrons, while single or multiple gamma rays in NC depended on the target of neutron capture. Therefore, the uniformity of the hit-PMT positions should be different for each reaction, which is called an isotropy. The isotropy is a powerful tool for the separation not only between CC/ES and NC but also between both of them and background events such as the decay of ^{208}Tl, which produces both electrons and gamma rays. As an isotropy parameter, a

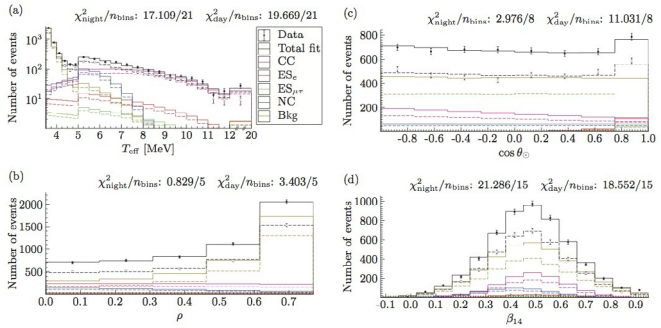

Fig. 6. Distribution of four variables with fitting results in Phase I data: (a) electron kinetic energy, (b) reconstructed radial position, (c) angle between the reconstructed event direction and solar direction, and (d) isotropy β_{14}. The hollow circles show day events, and the filled circles show night events [13].

linear combination of parameters $\beta_{14} \equiv \beta_1 + \beta_4$ is used, where

$$\beta_l = \frac{2}{N(N-1)} \sum_{i=1}^{N-1} \sum_{j=i+1}^{N} P_l(\cos\theta_{ij}). \qquad (14)$$

In this expression, P_l is the Legendre polynomial of order l, θ_{ij} is the angle between i-th and j-th hit-PMTs relative to the reconstructed event vertex, and N is the total number of hit-PMTs in the event. More isotropic events have lower (even negative) values of β_{14}.

The uncertainties of β_{14} were estimated by source calibrations, *i.e.*, ^{16}N (6.13 MeV gamma) and ^{252}Cf (neutron sources, emission of one or multi-gamma rays after capture). They were estimated to be $< 0.5\%$ in all phases.

4.5 Signal extraction

After applying several reduction steps to remove instrumental background, radioactivity events, and so on, signals of each reaction type were extracted by an extended maximum likelihood method. Here, the data set was divided into day and night times for CC and ES, whereas non-divided data were used for NC since neutrino oscillation is believed to cause the day-night asymmetry, and NC is free from neutrino oscillation. The above four variables, *i.e.*, the electron kinetic energy, the reconstructed radial position, the angle of the event direction, and the isotropy β_{14}, were fitted by the PDFs with a scaling factor given by the product of the total ^{8}B flux and the neutrino oscillation probability for CC and ES and only the total ^{8}B flux for NC. Figure 6 shows the fitting results for each variable in the Phase I data as an example.

5 Future prospects

One proposed future Cherenkov detector is Hyper-Kamiokande with a proposed location in the Kamioka mine. It is to have a megaton class of volume, and the analysis fiducial volume will be 560 kiloton, which is approximately 25 times larger than SK. It is designed as a multi-purpose detector and will be capable of making neutrino oscillation measurements (δ_{CP}, mass hierarchy, θ_{23} octant, etc.), studying atmospheric neutrinos and their oscillations, searching for proton decay, and detecting supernova neutrinos. Solar neutrino measurement is also an important physics motivation. One of the interesting topics in solar neutrinos in Hyper-Kamiokande is a detailed day-night asymmetry observation. The neutrino mass difference Δm^2_{21} has a 2σ level of tension in the results between solar neutrino global fit and KamLAND [14]. Since the day-night asymmetry is sensitive to this neutrino mass difference, the precise measurement in Hyper-Kamiokande may offer the possibility of separating these two mass difference values [15].

6 Conclusions

Analyses of water Cherenkov detectors used for solar neutrino observation are presented. Though the detection principle is simple, the analysis technique becomes quite sophisticated after many improvements. Such detectors have been one of the most powerful tools for revealing the neutrino properties and physics of the Sun. It can be expected that water Cherenkov detectors will produce fruitful results in this field in the future.

This work was supported by JSPS KAKENHI Grant Number 24103004.

References

1. K.S. Hirata *et al.*, Phys. Rev. Lett. **63**, 16 (1989).
2. M. Nakahata *et al.*, Nucl. Instrum. Methods A **421**, 113 (1999).
3. E. Blaufuss *et al.*, Nucl. Instrum. Methods A **458**, 636 (2001).
4. K. Abe *et al.*, Nucl. Instrum. Methods A **737C**, 253 (2014).
5. J. Hosaka *et al.*, Phys. Rev. D **73**, 112001 (2006).
6. J.P. Cravens *et al.*, Phys. Rev. D **78**, 032002 (2008).
7. K. Abe *et al.*, Phys. Rev. D **83**, 052010 (2011).
8. S. Fukuda *et al.*, Phys. Rev. Lett. **86**, 5651 (2001).
9. A. Renshaw *et al.*, Phys. Rev. Lett. **112**, 091805 (2014).
10. Y. Koshio, AIP Conf. Proc. **1666**, 090001 (2015).
11. B. Aharmim *et al.*, Phys. Rev. C **75**, 045502 (2007).
12. B. Aharmim *et al.*, Phys. Rev. C **81**, 055504 (2010).
13. B. Aharmim *et al.*, Phys. Rev. C **88**, 025501 (2013).
14. A. Gando *et al.*, Phys. Rev. D **88**, 033001 (2013).
15. Y. Koshio *et al.*, *The presentation in the 5th open meeting for the Hyper-Kamiokande project.*